NANO · MICRO small
www.small-journal.com

Microfluidic In Vitro Platform for (Nano)Safety and (Nano) Drug Efficiency Screening

*Yvonne Kohl, Margit Biehl, Sarah Spring, Michelle Hesler, Vladimir Ogourtsov, Miomir Todorovic, Joshua Owen, Elisabeth Elje, Kristina Kopecka, Oscar Hernando Moriones, Neus G. Bastús, Peter Simon, Tibor Dubaj, Elise Rundén-Pran, Victor Puntes, Nicola William, Hagen von Briesen, Sylvia Wagner, Nikil Kapur, Espen Mariussen, Andrew Nelson, Alena Gabelova, Maria Dusinska, Thomas Velten, and Thorsten Knoll**

Microfluidic technology is a valuable tool for realizing more in vitro models capturing cellular and organ level responses for rapid and animal-free risk assessment of new chemicals and drugs. Microfluidic cell-based devices allow high-throughput screening and flexible automation while lowering costs and reagent consumption due to their miniaturization. There is a growing need for faster and animal-free approaches for drug development and safety assessment of chemicals (Registration, Evaluation, Authorisation and Restriction of Chemical Substances, REACH). The work presented describes a microfluidic platform for in vivo-like in vitro cell cultivation. It is equipped with a wafer-based silicon chip including integrated electrodes and a microcavity. A proof-of-concept using different relevant cell models shows its suitability for label-free assessment of cytotoxic effects. A miniaturized microscope within each module monitors cell morphology and proliferation. Electrodes integrated in the microfluidic channels allow the noninvasive monitoring of barrier integrity followed by a label-free assessment of cytotoxic effects. Each microfluidic cell cultivation module can be operated individually or be interconnected in a flexible way. The interconnection of the different modules aims at simulation of the whole-body exposure and response and can contribute to the replacement of animal testing in risk assessment studies in compliance with the 3Rs to replace, reduce, and refine animal experiments.

1. Introduction

The need for new perspectives on in vivo-like and animal-free approaches for chemical and pharmaceutical safety assessment is growing both in the area of drug development and in risk assessment of chemicals Registration, Evaluation, Authorisation and Restriction of Chemical Substances (REACH).[1]

The main points of criticism regarding animal testing are related to not only ethical concerns but also the limited transferability to human physiology, due to significant differences in anatomy, organ structure, organ function, metabolism, and DNA-repair. As an ethical alternative to animal experiments, cellular organ-on-a-chip models represent a promising approach to better imitate the complex organization of organs and tissues, as they allow for 3D cellular organization with microfluidics simulating circulation in the body.[2–16]

Dr. Y. Kohl, M. Biehl, S. Spring, M. Hesler, Prof. H. von Briesen, Dr. S. Wagner, Dr. T. Velten, T. Knoll
Fraunhofer Institute for Biomedical Engineering IBMT
Joseph-von-Fraunhofer-Weg 1, Sulzbach 66280, Germany
E-mail: thorsten.knoll@ibmt.fraunhofer.de

Dr. V. Ogourtsov, M. Todorovic
Tyndall National Institute
University College Cork
Dyke Parade, Cork T12 R5CP, Ireland

Dr. J. Owen, Prof. N. Kapur
Institute of Thermofluids
School of Mechanical Engineering
University of Leeds
Leeds LS2 9JT, UK

The ORCID identification number(s) for the author(s) of this article can be found under https://doi.org/10.1002/smll.202006012.

DOI: 10.1002/smll.202006012

E. Elje, Dr. E. Rundén-Pran, Prof. E. Mariussen, Prof. M. Dusinska
NILU-Norwegian Institute for Air Research
Department for Environmental Chemistry
Health Effects Laboratory
Instituttveien 18, Kjeller 2007, Norway

E. Elje
Faculty of Medicine
Institute of Basic Medical Sciences
Department of Molecular Medicine
University of Oslo
Sognsvannsveien 9, Oslo 0372, Norway

K. Kopecka, Dr. A. Gabelova
Department of Nanobiology
Cancer Research Institute
Biomedical Research Center of the Slovak Academy of Sciences
Dubravska cesta 9, Bratislava 84505, Slovakia

O. H. Moriones, Dr. N. G. Bastús, Prof. V. Puntes
Institut Català de Nanociència i Nanotecnologia (ICN2)
CSIC and BIST
Campus UAB, Bellaterra 08193, Barcelona, Spain

Standardized cell-based assays do neither mimic the structural arrangement of different, sometimes highly specialized, cell arrangements within an organ or capture defined cell–cell interactions, which are important for physiological cell function. For example, mechanical stimuli in respiration[17] and intestinal peristaltic[6] have a decisive influence on the formation and regulation of a microphysiological environment.

Organ-on-chip models bring the advantage of reproduction of these microphysiological conditions in vitro and thus differ clearly from standardized cell-based assays, e.g., for safety testing described in current Organisation for Economic Co-operation and Development (OECD) guidelines.[18–23]

A challenge in the cultivation of complex organ models under physiologically relevant conditions is the maintenance of their function over a long period of time (days, weeks, months). Maintenance of organ models is enabled by microfluidic techniques to allow spatial control over fluids in µm-sized channels. Microfluidics can be exploited to enhance the physiological relevance of 3D cell models. During the last decade, lab-on-a-chip devices have been developed and used in various fields of life sciences.[3,5,9,14,24–36] Various in vitro models have already been combined with microfluidic systems (e.g., skin-on-chip, lung-on-chip, liver-on-chip, gut-on-chip, kidney-on-chip, retina-on-chip, and blood-brain-barrier-on-chip).[2,4,5,7,8,11,12,15,16,37–53] A much better mimicry of the human in vivo-like physiology can be achieved by merging different organs on chip.[5,10,26,34,54–59]

Microfabrication technologies offer new opportunities in the construction of miniaturized cell culture systems and their applications.[13,60–64] To improve the analytical capability of human organ-on-chip systems, various optical[65] or electrochemical biosensors[4,35,66] have been integrated in the devices to detect cytotoxic agents. Among the sensing technologies, impedance spectroscopy and transepithelial electrical resistance (TEER) measurements became the label-free method of choice for noninvasive determination of cell barrier integrity.[67–71] The need for live-cell imaging during cell cultivation has led to the development of systems allowing real-time visualization and characterization of cell behavior in parallel. These solutions include customized incubators with inverted fluorescence microscopes, compact microscopes that can be placed inside a laboratory incubator or completely automated cell culture observation systems.[72–75] All these solutions require costly and bulky lab equipment and do not allow cultivation and simultaneous optical analysis under dynamic flow conditions. The rapid progress in the development of new micro- and nanotechnologies together with more advanced cell culture models led to the development of a modular microfluidic platform for (nano)safety and (nano)drug efficiency screening.[76] This platform innovatively combines a microfluidic cartridge for cell cultivation with a miniaturized incubator microscope for optical analysis and electrodes for impedance measurements to determine cytotoxicity.

O. H. Moriones
Universitat Autònoma de Barcelona (UAB)
Campus UAB, Bellaterra, 08193, Barcelona, Spain
Prof. P. Simon, Dr. T. Dubaj
Institute of Physical Chemistry and Chemical Physics
Faculty of Chemical and Food Technology SUT
Radlinskeho 9, Bratislava 812 37, Slovakia
Prof. V. Puntes
Vall d'Hebron Institut de Recerca (VHIR)
Barcelona 08193, Spain
Prof. V. Puntes
Institució Catalana de Recerca i Estudis Avançats (ICREA)
Barcelona 08193, Spain
Dr. N. William, Prof. A. Nelson
School of Chemistry
University of Leeds
Leeds LS2 9JT, UK

2. Results and Discussion

2.1. Setup of the Microfluidic Platform

Before fabricating the microfluidic platform (a microfluidic cartridge combined with a miniaturized incubator microscope) a computational fluid dynamics (CFD) simulation was performed within Comsol Multiphysics to determine the requirements for the setup. A 3D advection-diffusion model was created and meshed using 2.3 million tetrahedral elements, confirmed to give a mesh-independent solution. The inlet and outlet channels and the cavity region, in which the cell models are cultured, was modeled, as shown in the cross-section of the model in **Figure 1**. Fluid flow with a density of 998 kg m^{-3}, dynamic viscosity of 8.9×10^{-4} Pa s, and volumetric inflow rate of 100 µL h^{-1} was predicted before simulating the transport of chlorpromazine, a soluble pharmaceutical compound (diffusion coefficient of 3.25×10^{-10} m^2 s^{-1}).[77] The no-slip and zero flux boundary conditions were applied at the geometry walls. The normalized concentration, c/c_o (where c_o is the inlet concentration and c is the local concentration) is shown on the surfaces of the cavity (Figure 1), demonstrating that the species is transported successfully to the cells within 700 s of entering the chip. No undesirable flow effects, such as fluid recirculation, were observed within the cavity geometry that could have disturbed the transport of species to the cells.

To confirm that hydrodynamic forces did not have a detrimental effect on the adherence of the cells to the surface of the microfluidic cavity or exceeded typical values seen in vitro which can indicate adverse impact on cell physiological behavior, the shear stress was calculated on the cavity surface using the CFD fluid flow model as shown in **Figure 2**. A peak shear stress of 0.0012 dyn cm^{-2} (for the study flow rate of 100 µL h^{-1}) was observed at the mid-point of the cellular surface, with the variation either side of this caused by the change in fluid velocity due to the transition from the entry and exit channels to the cavity. CFD results and analytical calculations for the shear stress (Equation (6)) showed excellent agreement (Figure 2d). The shear stress on the cells is shown to be below the critical values to cause adverse impact on cell behavior as cell viability with critical values taken as 5 dyn cm^{-2} (A549), 0.33 dyn cm^{-2} (HepG2), and 2 dyn cm^{-2} (TH-1)[78–80] and is in line with other studies within the field.[81]

2.1.1. Microfluidic Cartridge

The core part of the microfluidic cartridge is a custom-designed microfabricated silicon chip. It comprises a microcavity with

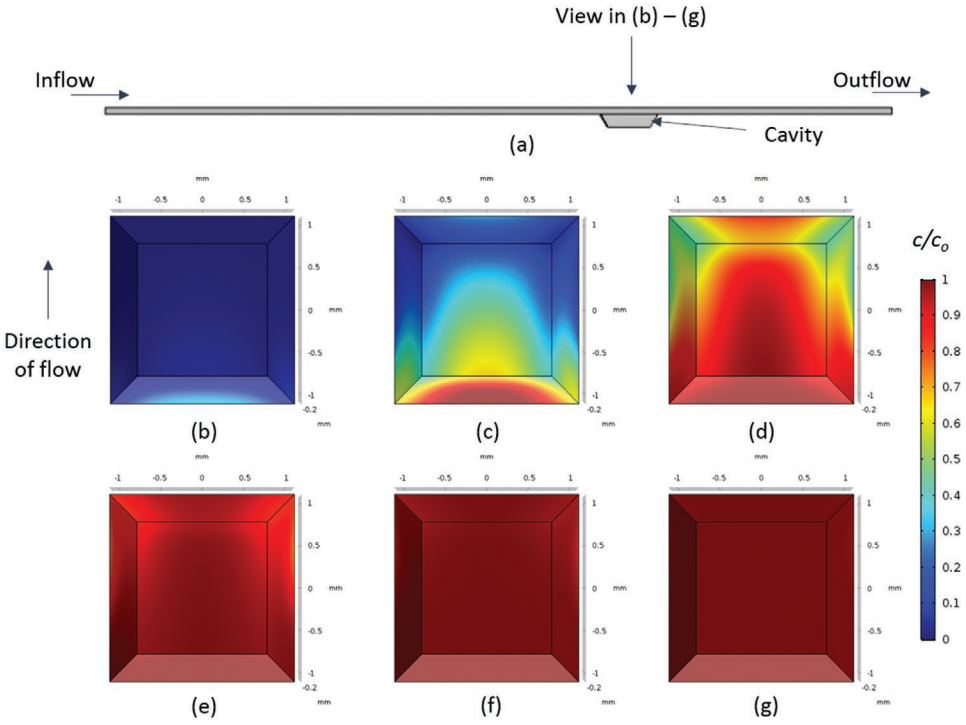

Figure 1. CFD simulation of fluid flow and species transport through a microfluidic channel. a) Cross-section of the geometry and the normalized concentration of species at the cavity walls after b) 400 s, c) 500 s, d) 600 s, e) 700 s, f) 800 s, and g) 900 s (bottom edge of (b)–(g) is left hand edge of cavity in (a)).

a volume of ≈2.5 µL (**Figure 3**a), in which the cells are cultivated on a thin transparent membrane made of silicon nitride that comprises a regular array of microholes (Figure 3b). With these microholes, the microfluidic cartridge can be used as a minaturized device for barrier models with dense cell layers on the silicon nitride membrane. The principle of the barrier model cultivation on the microhole membrane is similar to that of commercially available larger coculture systems, as, e.g., the Transwell system. In contrast to cell culture inserts used in static cultures, the integrated microfluidic channels

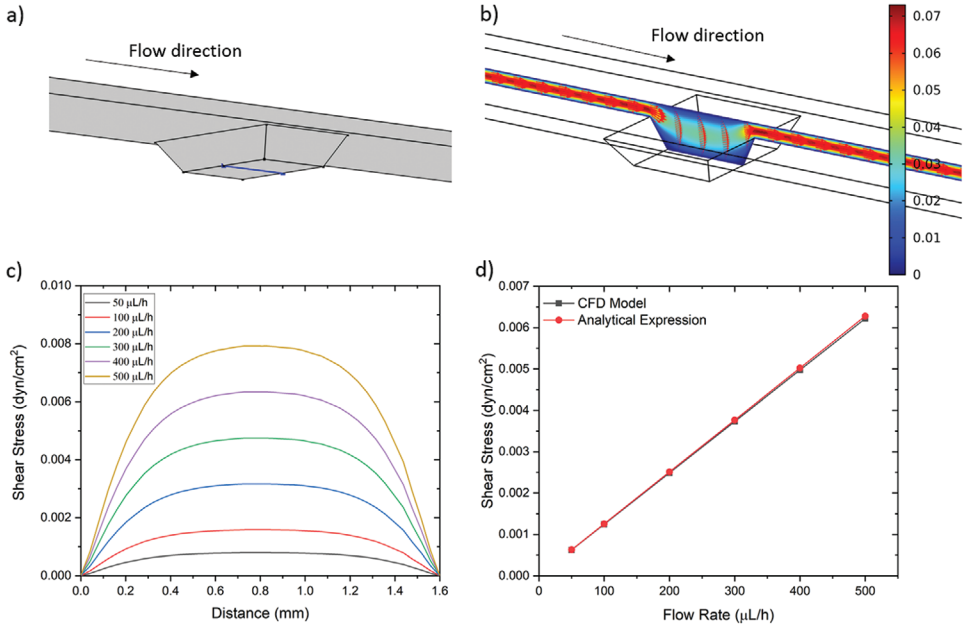

Figure 2. CFD prediction of shear stress in the microfluidic channel cavity at flow rates of 50–500 µL h^{-1}. a) Location along the bottom surface of the cavity where shear stress was determined. b) Flow velocity (mm s^{-1}) through the center of the microfluidic cell at a flow rate of 100 µL h^{-1}. c) Predicted shear stress in the cavity, where distance on the *x*-axis refers to the position along the cavity wall in the direction of flow. d) Comparison of the mean shear stress predicted using CFD with the average shear stress determined by an analytical equation for calculating shear stress in microfluidic channels.

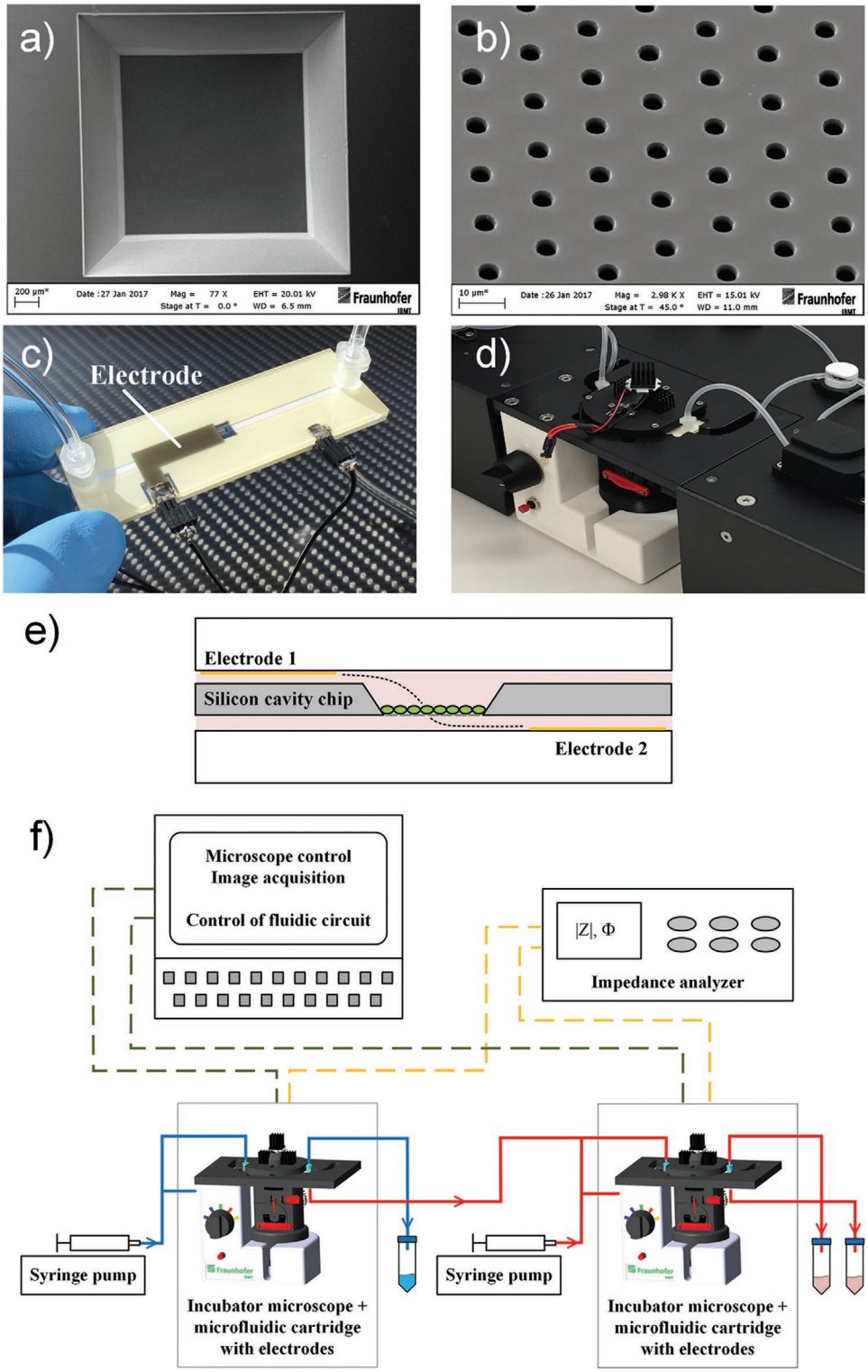

Figure 3. Setup of microfluidic cartridge and miniaturized incubator microscope platform. a) SEM image of microcavity with microhole array membrane (1.6 mm x 1.6 mm). b) SEM image of microhole array with hole distance 10 µm. c) Microfluidic cartridge with connected tubing and cables for impedance measurement. This cartridge is integrated in the miniaturized incubator microscope. d) Incubator microscope with inserted microfluidic cartridge and lid, for bright field imaging and cell cultivation under controlled temperature. e) Schematic illustration of the microfluidic cartridge. The electrodes (yellow) are positioned in the two fluidic channels. The electric current flows between the electrodes through the pores in the membrane (dashed line). f) Schematics of experimental setup with two platform modules for parallel or serial operation.

allow for the cultivation of the cells under dynamic flow conditions. Figure 3c shows the assembled microfluidic cartridge with the integrated silicon chip. The gold electrodes in the microchannels are connected with the impedance measurement setup that detects the impedance spectrum between the two channels and through the membrane with the cell layer (Figure 3c). An exploded view drawing of the individual components of the microfluidic cartridge can be found in Figure S1 in the Supporting Information.

2.1.2. Miniaturized Incubator Microscope

The developed miniaturized incubator microscope allows for continuous real-time monitoring of cell characteristics, such as morphology, cell growth, and cell response in the microfluidic cartridge. The inserted microfluidic cartridge is connected with an adapter for temperature regulation (Figure 3d). Components for temperature regulation (Peltier elements, Negative temperature coefficient thermistors) and the light source for bright-field illumination are integrated in the fixation lid on the microfluidic cartridge (Figure 3d). The horizontal assembly protruding from the side of the microscope tube comprises illumination components for fluorescence imaging. The compact microscope has a field of view of 1.4 mm x 1.05 mm and a magnification of 4.4. With the restricted numerical aperture (N.A. = 0.208) of the small objective lens a point-shaped object fluorescing at a wavelength of 610 nm will theoretically be depicted with a full width at half maximum of 1.5 µm, which is in reasonable accordance with the camera pixel size of 1.25 µm.

2.1.3. System Integration of the Microfluidic Platform

Each module of the microfluidic platform comprises a fluidic system with valves, tubing, and pumps that is integrated with the miniaturized incubator microscope and the microfluidic cartridge. Cell suspension, reagents, and cell culture medium are delivered to and led away from the silicon microcavity via flow channels by means of a syringe pump. During cell cultivation, fresh cell culture medium is constantly delivered to the cells in the microcavity. The electrodes for impedance measurement are positioned in the two fluidic channels and the electric current flows through the pores in the membrane (Figure 3e). Each platform module, equipped with an imaging module and fluidic components, can be operated independently or connected with other platform modules operating in parallel or in series. Control of the imaging modules and time-lapse imaging is performed by a LabView program. The electrodes of both microfluidic modules are connected with the LabView-controlled impedance measurement system for parallel recording of the impedance data (Figure 3f).

2.2. Nanoparticle Synthesis and Characterization

Silver nanoparticles (Ag-NP), fluorescently labeled silica nanoparticles with fluorescein isothiocyanate (FITC) (SiO_2-FITC-NP), titanium dioxide nanoparticles (TiO_2-NP), and gold NPs functionalized with polyethylene glycol (PEG)-SH MW5000 (Au-PEG-NP) were prepared following well-known standard procedures. A summary of the physical and chemical characteristics of the NPs used in this study is presented in Figure S2 and Table S1 in the Supporting Information.

2.3. In Vitro Studies on the Microfluidic Platform

2.3.1. Cell Characteristics on the Microfluidic Platform

The suitability of a silicon nitride membranes as a surface for cell cultivation has been demonstrated previously.[82] To verify the suitability of the miniaturized incubator microscope as a microwell for cultivation, three human cell lines A549 (lung), HepG2 (liver), and TH-1 (kidney) were used as example models for studying adhesion and cultivation, cell morphology (**Figure 4**a) as well as the percentage of viable and dead cells (**Table 1**). During cell cultivation, the platform is maintained at a constant temperature of 37 ± 0.5 °C. All studied cell types successfully adhere on the silicon nitride membrane and proliferate. Cells cultivated on the platform show no differences in morphology, migration, adherence or proliferation rate compared with cultivation under static conditions. A549 and TH-1 cells are characterized by a spindle-shaped morphology and HepG2 by a round shape morphology. The results of cell viability assessment using FDA/PI (fluorescein diacetate/propidium iodide) staining are comparable under microfluidic and static conditions, for all three tested cell types (Table 1).

After adhering to the surface of the silicon nitride membrane, the cells form a dense cell layer and, depending on cell type, specific cell junctions (tight junctions) are formed. This cellular changes can be quantified noninvasively via impedance measurement using the gold electrodes positioned in the upper and lower fluidic channel. From the time of seeding, TH-1 cells proliferate in the cartridge as seen by an impedance change of 1061 Ω after 12 h and 1275 Ω after 48 h (Figure 4b). In the case of the A549 cells, the impedance change is 1552 Ω after 12 h and 1625 Ω after 48 h. Although, HepG2 cells appear to proliferate more slowly in the cartridge, as seen by an impedance change of 710 Ω after 48 h (Figure 4c), they still continue to grow and proliferate. For instance, after 5 d (120 h) HepG2 cells show an impedance change of 990 Ω (Figure 4c).

2.3.2. DNA Stability of Cells under Microfluidic Conditions

HepG2 cells were cultured in the closed cartridge under fluidic conditions before being subjected to the enzyme-linked version of the comet assay for analyzing DNA stability (DNA strand breaks and oxidized base lesions) (**Table 2**). Previous live/dead staining (data not shown) confirms that their cell viability was high enough for the cells to be used for the comet assay (Figure 2). The basal DNA damage of HepG2 cells in the microfluidic system is slightly higher than for the case where cells were cultured in standard static 2D systems

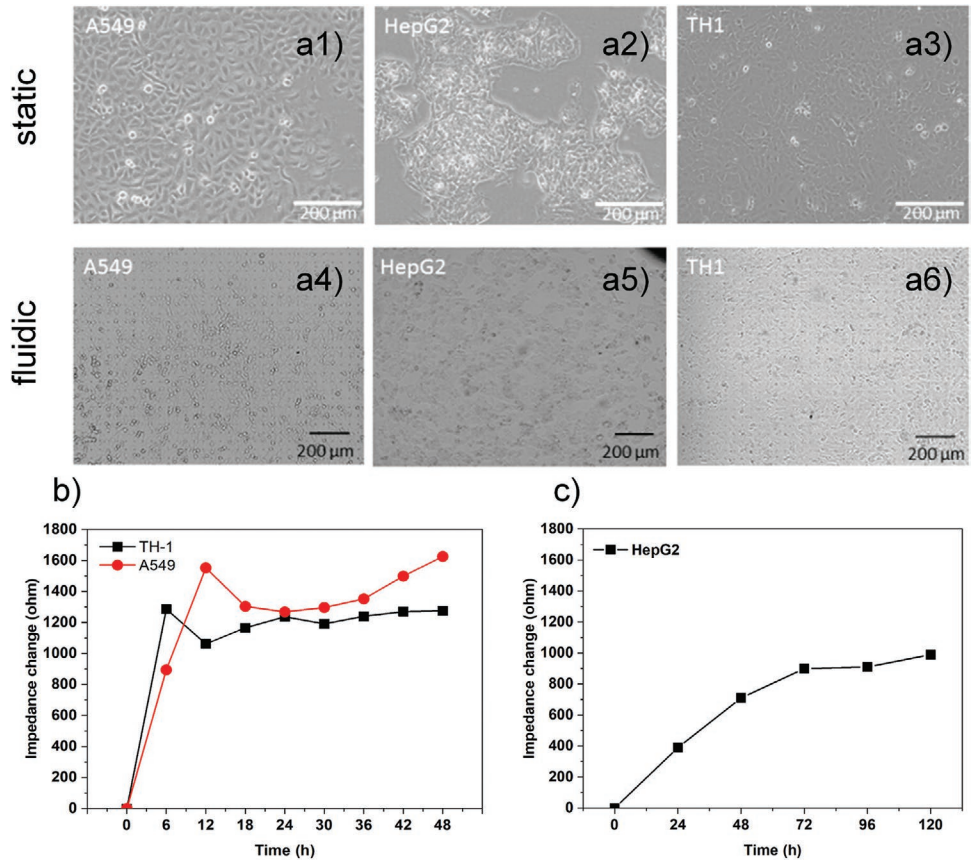

Figure 4. Growth behavior of the human cells lines on the miniaturized incubator microscope platform. a) Bright-field imaging of different cell types with different morphologies, cultured under static and fluidic conditions. Human epithelium of lung (A549), liver (HepG2), and kidney (TH-1) were cultured under standard static conditions (T25 flask) and in the developed cartridge under fluidic conditions (medium flow 100 µL h^{-1}). After 24 h the statically cultured cells were imaged via standard microscope (IX81, Olympus) and the cells in the cartridge via miniaturized incubator microscope. No morphological differences were identified between cells cultivated under static compared to fluidic culture conditions. b,c) Impedance analysis of different epithelial cell lines during their culture in the microfluidic cartridge. The human cell lines b) TH-1 and A549 and c) HepG2 were cultured in the developed cartridge under fluidic conditions (medium flow 100 µL h^{-1}). Impedance analysis at 10 kHz frequency was performed in line with the cell cultivation over a period of b) 48 h in case of TH-1 and A549 and c) 120 h in case of HepG2. For all cell types cell proliferation resulted in an increase of the impedance.

(96-well plate).[83] Fluidic conditions induce a slight, nonsignificant increase in DNA strand breaks (SBs) but no increase in oxidized DNA base lesions (formamidopyrimidine Fpg) (Table 2). The positive control (H_2O_2 for DNA SBs and Fpg for oxidized base lesions) induce DNA damage as expected (Table 2).

Table 1. Proportion of viable and dead cells after 24 h cultured under static and fluidic conditions. Human cell lines (A549, HepG2, and TH-1) were cultured under standard static conditions (T25 flask, incubator, 37 °C, 95% humidity, 5% CO_2) and in the developed cartridge under fluidic conditions (medium flow 100 µL h^{-1}, 37 °C). After 24 h in culture the viability of the cells was analyzed via live/dead staining.

Cell line	Culture condition	Amount of cells [%]	
		Viable	Dead
A549	Static	97.0 ± 1.0	3.0 ± 2.5
A549	Fluidic	95.7 ± 3.3	4.3 ± 3.3
HepG2	Static	92.0 ± 2.6	8.0 ± 1.6
HepG2	Fluidic	96.0 ± 4.9	4.0 ± 2.9
TH-1	Static	95.7 ± 1.2	4.3 ± 1.0
TH-1	Fluidic	94.0 ± 3.6	6.0 ± 3.6

Table 2. Comet assay results of HepG2 cells cultured under static and fluidic conditions. The cells were exposed to fresh medium under static (96-well plate) and fluidic conditions (medium flow 100 µL h^{-1}, 37 °C) for 24 h before measurement of DNA damage via comet assay. H_2O_2 (100×10^{-6} M) was used as a positive control for DNA strand breaks (DNA SB). Results show mean ± standard deviation of three independent experiments. No net Fpg was determined after H_2O_2 exposure.

DNA damage	Culture condition	% DNA in tail	
		Cell medium	H_2O_2
DNA SBs	Static	5.0 ± 2.3[a),b)]	95.5 ± 0.2[c)]
DNA SBs	Fluidic	10.3 ± 5.2	83.3 ± 9.0
Net Fpg	Static	3.7 ± 2.1[a),b)]	–
Net Fpg	Fluidic	11.6 ± 10.7	–

[a)]Elje et al.[83]; [b)]$n = 9$; [c)]Elje et al.[84]

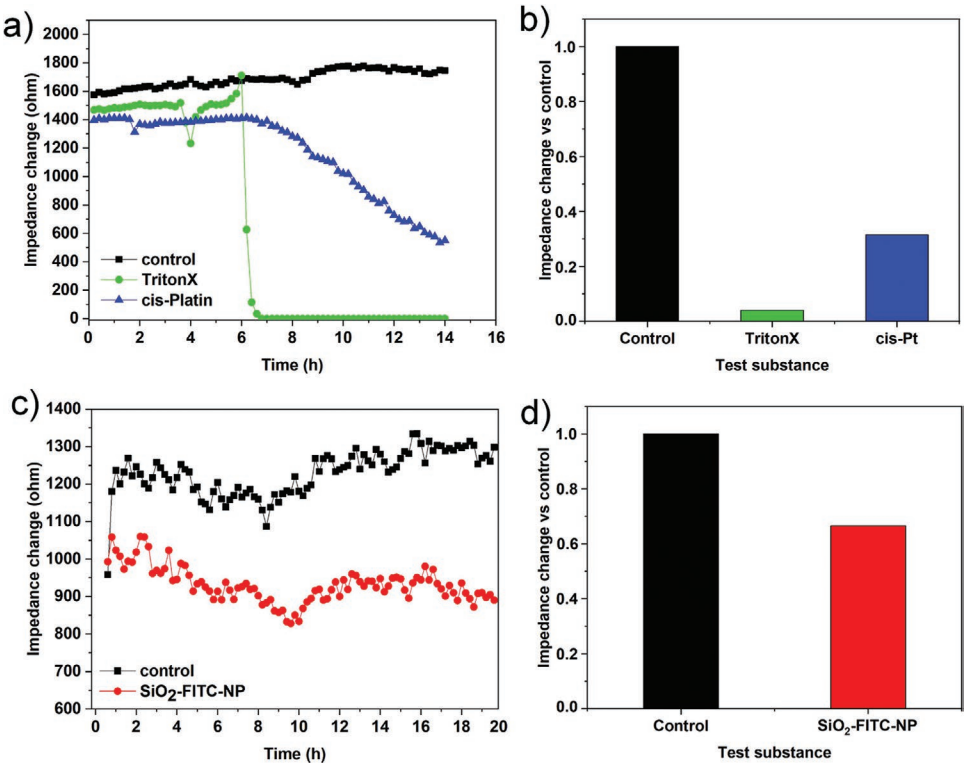

Figure 5. In vitro effects of reference chemicals and SiO_2–FITC-NP under microfluidic conditions. a) Impedance analysis of A549 cells at 10 kHz frequency during exposure to *cis*-Pt (concentration 20 µg mL^{-1}, blue line) in the microfluidic cartridge (flow rate 100 µL h^{-1}). Nonexposed cells (black) and Triton X exposed cells (green) act as negative and positive controls, respectively. b) Impedance change after 48 h exposure of A549 cells with *cis*-Pt, Triton X, and cell culture medium (control). c) Impedance analysis at 10 kHz frequency of TH-1 cells during their exposure to SiO_2–FITC-NP (100 µg mL^{-1}) in the microfluidic cartridge (flow rate 100 µL h^{-1}). Nonexposed cells (black) act as negative control (control). d) Impedance change after 48 h exposure of TH-1 cells with SiO_2–FITC-NP and cell culture medium (control).

2.3.3. Validation with Reference Chemicals under Microfluidic Conditions

Before the platform was used for in vitro studies with nanomaterials, the system was validated with reference chemicals. For this purpose A549 cells (2×10^6 mL^{-1}), cultured in the microfluidic platform, were exposed to *cis*-Platin (*cis*-Pt, 20 µg mL^{-1}), a cytostatic drug whose effect is based on the inhibition of DNA replication by crosslinking of two adjacent guanine bases of a DNA strand. Impedance measurements during the cultivation of A549 cells in the cartridge show a significant decrease of the impedance after 48 h exposure to *cis*-Pt (**Figure 5**a, blue line), in contrast to the nonexposed cells (Figure 5a, black line). Over a period of 2.5 h the impedance is decreased from 1404 to 550 Ω (39.2%) (Figure 5a, blue line). Whereby the nonexposed control remains stable between 1568 Ω (start of the measurement) and 1745 Ω (2.5 h) (Figure 5a, black line). Also in the case of Triton X-100 (positive control), the impedance of the cells decreases significantly compared to the control (Figure 5a, green line). The value of Triton X is reduced over this period (2.5 h) by 100% from 1463 to 0 Ω.

EC_{50} value (half-maximal effective concentration) for *cis*-Pt (24 h) in A549 cells is determined to be 25 µg mL^{-1} under static conditions (data not shown). Under fluidic conditions *cis*-Pt induces the same effect as determined under static conditions (Figure 5b).

2.3.4. In Vitro Effect of SiO_2-FITC-NP under Microfluidic Conditions

TH-1 cells (2×10^6 mL^{-1}), cultured in the microfluidic platform, were exposed to silica–FITC core labeled nanoparticles (SiO_2-FITC-NP, 100 µg mL^{-1}). Impedance measurements during the cultivation of TH-1 cells in the cartridge show no significant decrease in impedance after the exposure to SiO_2-FITC-NP at 24 h (Figure 5c, red line), compared to nonexposed cells (Figure 5c, black line). Cytotoxicity studies with SiO_2-FITC-NP under static conditions demonstrate no toxic effects up to a concentration of 15.3×10^{-3} M (922 µg mL^{-1}) over a duration of 24 h (data not shown). Under fluidic conditions, SiO_2-FITC-NP induces the same effect as determined under static conditions (Figure 5d).

2.3.5. In Vitro Effect of SiO_2-FITC-NP on the Microfluidic In Vitro Platform

A performance test for hazard screening via the interconnected microfluidic in vitro platform (**Figure 6**a) was performed with SiO_2–FITC-NP. HepG2 cells and TH-1 cells were cultured in individual microfluidic cartridges (module 1 and module 2), interconnected via microfluidics, simulating in vivo-like physiology (Figure 6b). SiO_2–FITC-NP were injected

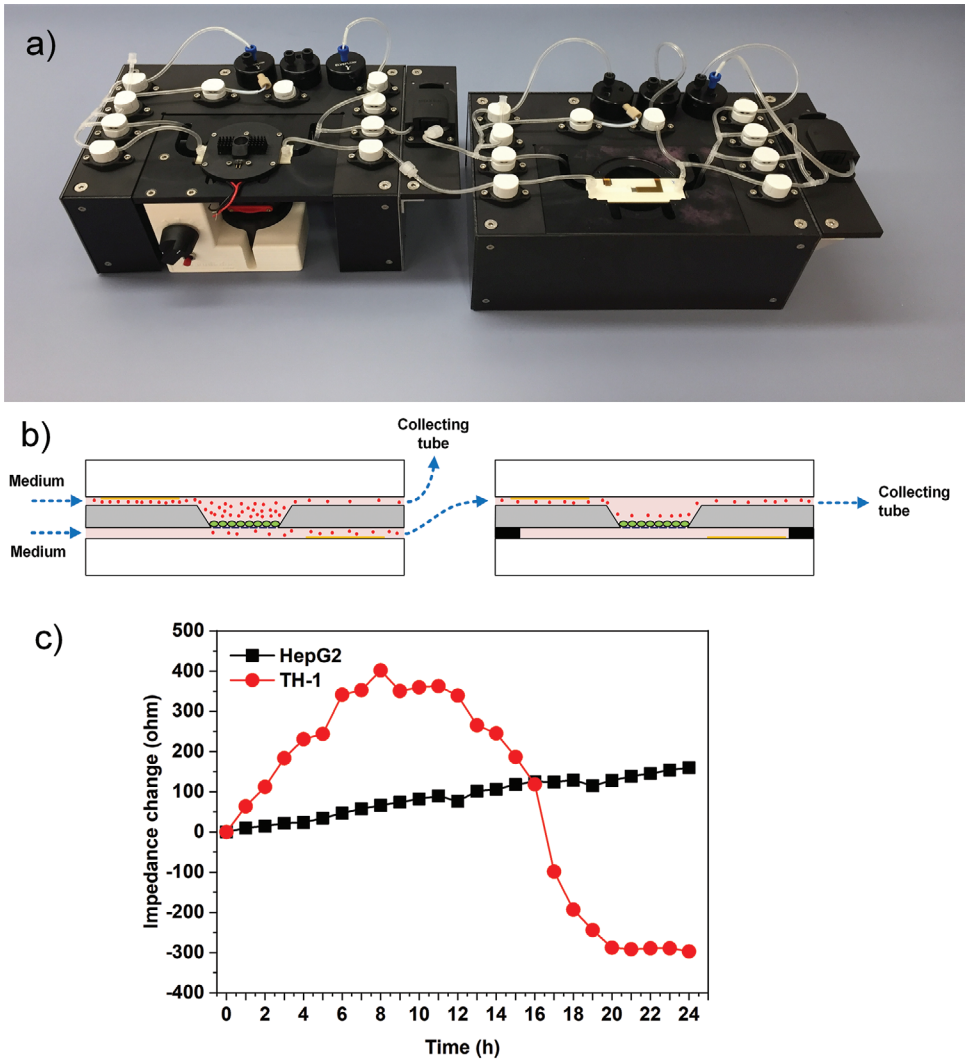

Figure 6. In vitro effects of SiO_2–FITC-NP under microfluidic conditions in the interconnected platform. a) Two interconnected microfluidic platforms. Right module with lid removed to show the microfluidic cartridge. b) Schematic illustration of the fluidics interconnection. c) Impedance analysis of HepG2 cells (module 1, black line) and TH-1 cells (module 2, red line) at 10 kHz frequency during exposure to SiO_2–FITC-NP (concentration 100 µg mL^{-1}) on the two interconnected microfluidic platforms (flow rate 100 µL h^{-1}). The diagram displays the impedance over time of exposure.

in module 1 (HepG2 cells) and electrical impedance measurements were performed in both modules (Figure 6c). After the addition of SiO_2–FITC-NP in module 1, the impedance of the HepG2 cells increase constantly due to cell proliferation, which does not indicate any cytotoxic effect on the HepG2 cells. 12 h after the addition of SiO_2–FITC-NP, the impedance in module 2 (TH-1 cells) decreased, indicating the induction of a cytotoxic effect in the TH-1 cells (Figure 6c). The results indicate that the SiO_2–FITC-NP were transported from module 1 to module 2 and the effect was cell type-dependent. It is also possible that the liver cells that interact first with the SiO_2–FITC-NPs release a messenger substance, for example cytokines, which are transported to module 2, triggering a cytotoxic effect in the TH-1 cells. After demonstrating the detection of dose-dependent, organ-specific effects, with reference chemicals and NPs, the qualification of the system for transport studies was studied.

2.3.6. Transport of Au-NP over Bronchial Epithelial Cell Barrier under Microfluidic Conditions

The microholes in the silicon nitride membrane enable the transport of NPs through the membrane to the bottom channel. This brings the following advantages: a) transfer of the NPs to a second sensing module by interconnecting; b) realization of transport studies with NPs, but also drugs and chemicals; and c) sampling of transported NPs for physicochemical characterization. The impedance data give information on the coverage of the microholes by the cells and the condition of the cells in case of NP exposure.

The transport of Au-PEG-NP over a cell barrier was studied in the human bronchial epithelial cell line, 16HBE, which was cultured under both static and fluidic conditions. It is well known that 16HBE cells form tight junctions and produce a dense, cellular barrier in cell culture inserts. TEER serves as an

Table 3. Au elemental distribution of PEG-Au NPs after transport studies under static conditions. Via ICP-MS Au elemental distribution in apical cell culture medium, basolateral cell culture medium, and cell lysates were determined after the exposure of Au-PEG-NPs (5 µg mL^{-1}) to human bronchial epithelial cells (16HBE) under static conditions in a Transwell setup. For each elemental part a blank (absence of cells, presence of Au-PEG-NP) and a control (presence of cells, absence of Au-PEG-NP) were measured. The amounts of Au-PEG-NPs are expressed as total µg Au.

Elemental Au [µg]	Exposure time		
	4 h	24 h	48 h
Static apical			
Control	<0.125[a)]	<0.125[a)]	<0.125[a)]
Blank	1.9 ± 0.0[b)]	1.6 ± 0.0[b)]	1.65 ± 0.05[b)]
Au-PEG-NP	2.57 ± 0.21	1.93 ± 0.12	1.63 ± 0.05
Static basolateral			
Control	<0.125[a)]	<0.125[a)]	<0.125[a)]
Blank	1.5 ± 0.05[b)]	1.5 ± 0.0[b)]	1.55 ± 0.0[b)]
Au-PEG-NP	<1.2	<1.2	<1.2
Static cell lysate			
Control	<0.125[a)]	<0.125[a)]	<0.125[a)]
Blank	0.29 ± 0.07[b)]	0.17 ± 0.003[b)]	0.16 ± 0.005[b)]
Au-PEG-NP	0.32 ± 0.01	0.29 ± 0.03	0.41 ± 0.03

[a)]Controls were below the detection limit; [b)]In the case of the blanks, levels of Au around 0.165 µg were systematically measured, which are indicative enough of the presence of Au in the samples.

indicator for the formation of tight junctions and the density of this cellular barrier.[69,85] After 4 d of cultivation in a 24-well cell culture insert, the TEER of 16HBE reaches a constant value of 688 ± 22 Ω. This is consistent with data from other studies.[85] In the microfluidic system the impedance value was also constant before cell exposure was started.

After exposure of 4, 24, and 48 h the amount of Au was analyzed by induced coupled plasma-mass spectroscopy (ICP-MS) and atomic spectroscopy. The analysis of elemental gold after static exposure in cell culture insert shows that even after 48 h most of the particles remain still on the apical side of the 16HBE cellular barrier. The NP concentration is reduced over time. However, the amount of Au on the basolateral side was still below the detection limit after 48 h (**Table 3**). In the cell lysate, only a small increase in the amount of Au could be detected (0.41 ± 0.03 µg after 48 h exposure of 5 µg mL^{-1} Au-PEG-NP). Under fluidic conditions, 16HBE were exposed with Au-PEG-NPs (5 µg mL^{-1}) (flow rate of 100 µL h^{-1}, n = 2). As in the static setup, a time-dependent reduction of the Au amount in the apical medium could be detected (3.76 ± 0.26 µg L^{-1} after 4 h, 3.06 ± 0.02 µg L^{-1} after 24 h, 2.58 ± 0.25 µg L^{-1} after 48 h). Thus, the uptake of Au-PEG-NP into the cells could be shown under static and fluidic conditions, which proves that the developed microfluidic cartridge is suitable for uptake and transport studies.

The presented results show that the developed microfluidic platform can be used for several applications in the field of drug testing and (nano)toxicity testing. Standard assays, which are commonly performed under static conditions in multiwell plates, were successfully modified and adapted to the dynamic conditions of the microfluidic platform. The use of the microfluidic platform is independent of the chosen cell line. Direct control of the cells cultivated in the microfluidic cartridge was obtained by real-time imaging and real-time impedance measurements.

Most other approaches either do not provide real-time imaging of cells or require the use of a lab incubator to cultivate the cells in the microfluidic devices.[86–88] The microfluidic platform provides both the necessary environment for cell cultivation and the components for real-time electrical and optical detection of the cell's growth status. Thus, the platform does not require any additional microscope or lab incubator. It meets the need for flexible technologies in the field of organ-on-chip devices.[89,90]

The innovative flexibility of the microfluidic platform was shown to enable real-time investigations at the single and multicellular level, to study different endpoints, as cytotoxicity, genotoxicity, and toxicological pathways. This multimodular approach allows different aspects of one or several processes to be interrogated and analyzed simultaneously. The advantage of the developed platform is the application as a serial or parallel platform and freedom to select the number of platforms to interconnect with each other. Real-time TEER measurements of the formed cell layers inside the microfluidic cartridge has been successfully combined with real-time bright-field and fluorescent imaging of the cells in the individual modules. The combination of fluidic systems with biosensors, such as impedance spectroscopy, and microphysiometry as well as physiology identification and quantification of the expression of specific cellular markers is the next level of lab-on-chip devices.[69,9,91] The developed microfluidic platform follows this approach. In contrast to other existing microphysiological systems,[86,92–94] the described cartridge fabrication can easily be adapted for higher numbers. Most components, such as the cartridge bottom and lid and adhesive foils for microchannels are suitable for mass fabrication and (semi)automated assembly. This aspect is important for increased acceptance and future use and marketing of those microphysiological systems beyond the research and development area.

3. Conclusion

The goal of this study was to develop a more efficient, modular microfluidic in vitro platform for (nano)safety and (nano) drug efficiency screening and to provide "how" and "why" answers for the fundamental processes of human response to NPs. For this purpose, an innovative modular microfluidic platform was developed with the capability of reliably analyzing bio-nano-interactions in real-time. The developed microfluidic in vitro platform allows bright field and fluorescent imaging in parallel with impedance measurements. This enables the determination of interwell cell distribution, investigation of changes in cell morphology and the detection of fluorescent dyes, reporter genes or cell markers. The developed microfluidic integration provides the infrastructure for the cultivation of artificial tissues on-chip under physiological conditions. The

interconnection of the different modules aims at the simulation of whole-body exposure and response. The platform is cell-type independent and can flexibly be interconnected as a serial or parallel system. Due to the array structure of the microholes on the microfabricated transparent membrane the system could also be used for studies on a single cell level.[95]

After successful validation with a variety of cell lines, future steps in development of this infrastructure include combination with other cell models, such as human induced pluripotent stem cells or reporter cells, for example. The modular platform allows the generation of a more reliable cell-based assay data for many types of applications, such as safety analysis (endpoint and toxicokinetic studies) including food allergy studies, disease modeling, immune therapy development, functional food development, and drug efficacy testing in the pharma area.

In all fields of application this in vitro platform contributes to the replacement of animal testing in risk assessment studies in compliance with the 3Rs to replace, reduce, and refine animal experiments. By simulating the in vivo-like physiological conditions the microfluidic in vitro platform meets the need for new perspectives on in vivo-like and animal-free approaches for chemical and pharmaceutical safety assessment.

4. Experimental Section

Fluid Dynamics Simulation: CFD simulations of fluid flow at a flow rate of 100 µL h^{-1} and species transport through the microfluidic channel, using the methodology applied to study flow through a similar microfluidic geometry by the authors,[96] confirmed no undesirable flow characteristics were observed in the microfluidic channel and cell cavity. The concentration of species within the cavity reached that of the inflow concentration after approximately 700 s, a short time compared to the overall timescale of the exposure period (24 h) during an experiment. CFD simulations were completed using COMSOL Multiphysics v5.3a to predict fluid flow and chemical species transport within the microfluidic cell. The Navier–Stokes equations for incompressible, steady-state, isoviscous fluid flow through the microfluidic channel with no gravity effects were solved

$$\nabla \cdot \mathbf{u} = 0 \tag{1}$$

$$\rho(\mathbf{u} \cdot \nabla)\mathbf{u} = -\nabla p + \mu \nabla^2 \mathbf{u} \tag{2}$$

where $\mathbf{u}$ is the fluid velocity vector (m s^{-1}), p is the pressure (Pa), μ is the dynamic viscosity (Pa s), and ρ is the pressure (kg m^{-3}).

Time-dependent species transport through the microfluidic channel was solved using the advection-diffusion transport equation

$$\frac{\partial c}{\partial t} = D\nabla^2 c - \mathbf{u} \cdot \nabla c \tag{3}$$

where c is the species concentration (mol m^{-3}) and D is the diffusion coefficient of the dilute species (m^2 s^{-1}).

The shear stress in the channel was calculated to determine if the fluid flow influenced the adherence of the cells to the surface of the microfluidic cavity. The wall shear stress was calculated along the cavity wall, shown in Figure 2, using the following equation

$$\tau = \mu \cdot \dot{\gamma} \tag{4}$$

where τ is the shear stress (Pa), expressed as dyn cm^{-2} (1 Pa = 10 dyn cm^{-2}), and $\dot{\gamma}$ is the fluid shear rate (s^{-1}) equivalent to the velocity gradient perpendicular to channel surface in the y direction

$$\dot{\gamma} = \frac{du}{dy} \tag{5}$$

where u is the magnitude of flow velocity (m s^{-1}).

For 2D microfluidic channels, the wall shear stress can be estimated using the following expression[81]

$$\tau = \frac{6\mu Q}{h^2 w} \tag{6}$$

where Q is the flow rate (m^3 s^{-1}), h is the channel height (m) and w is the channel width (m).

Microfluidic Cartridge: The microfluidic cartridge was designed as an adaptable modular device in microscope slide format. The cavity is fabricated by wet chemical etching of silicon in potassium hydroxide. The membrane has a regular array of microholes with a hole diameter < 5 µm that is fabricated by reactive ion etching of the silicon nitride layer. The cavity chip with the porous membrane is placed between two microfluidic channels, each having a cross section of 0.6 mm^2. The microfabricated silicon-based cavity chip was integrated into a microfluidic cartridge, which was made up from two injection-molded polystyrene plates with Luer adapters (Greiner Bio-One), a 0.5 mm thick ceramics plate (CoorsTek, USA) and two layers of medical grade pressure-sensitive adhesive (AR 90106, Adhesives Research, Ireland). The cartridge has a symmetrical structure with the cavity chip in the center. Two microchannels are defined by the adhesive layer that connects the polystyrene plates with the 0.5 mm thick aluminum oxide ceramics plate. This plate has an opening for the insertion of the silicon cavity chip and separates the two microchannels both electrically and fluidically. Thin film gold electrodes for impedance sensing were deposited by sputtering onto two polystyrene parts that cover two flow channels.

Miniaturized Incubator Microscope: The miniaturized microscope comprises two subsystems: the imaging module and the heating unit that is used for temperature control of the microfluidic cartridge. Based on a CMOS (complementary metal-oxide-semiconductor) camera, the imaging module was specifically designed for the microfluidic cartridge and the implementation into the microfluidic platform. Components with high accuracy requirements for the optical path were fabricated mechanically by computerized numeric control milling and anodized. Other components, including the housing for the light-emitting diode (LED) light source, electronics and the socket for the board-level camera, were manufactured by 3D-printing. The imaging module comprises a lens (Lensagon B10M7224, Lensation, Germany), a color CMOS camera (UI-3592LE-C, Image Development Systems, Germany), a fluorescence 4-band-filter-set for 4',6-diamidin-2-phenylindol, FITC, tetramethylrhodamine, and Cy5 (Semrock, USA) as well as the LEDs. An LED in the amber range (588 nm, LUXEON Z LXZ1-PL01, LUMILEDS, USA) was used as a light source for transmission bright-field imaging. Fluorescence imaging was realized with Köhler incident light illumination using four LEDs (LUXEON UV U Line, LUMILEDS, USA) with excitation wavelengths in the UV (385 nm), blue (470 nm), and lime range (567.5 nm), which were mounted on a metal core printed circuit board and controlled by multi-LED driver electronics. A LabView program was developed for the optical monitoring and analysis of cells in the microcavity. The software controls all LEDs and the CMOS camera, thus allowing for video recording and time-lapse imaging in bright-field and fluorescence mode.

All components for temperature control, together with bright-field illumination, were integrated into the lid of the microscope. Two Peltier elements, each equipped with a heat sink, are in thermal contact with the top part of the microfluidic cartridge, and an negative temperature coefficient-temperature-sensor measures the temperature at the surface of the microfluidic cartridge. A commercial Peltier-controller (TLK 33, Sika GmbH, Germany) evaluates the signals from the temperature sensor and controls direction and intensity of the current through the Peltier elements. Temperature during cultivation was measured in a test cartridge with an integrated Pt-100 temperature sensor. During cell cultivation the temperature was maintained at a value of 37 ± 0.5 °C. Stability of pH (between 7.4 and 7.8) and sufficient oxygen concentration in the

cartridge were also measured in the test setup. Samples taken from the microchannels at different timepoints were analyzed with a Portamess pH meter and oxygen concentration was measured using oxygen nanoprobes and a fiber-optic oxygen sensor from PyroScience (Germany).

Fluidic Circuit: Commercially available fluidic and microfluidic components were selected to guarantee a maximum flexibility for the platform operation. These commercial components comprise solenoid pinch valves (Bio-Chem Valves, USA), syringe pumps (New Era Pump Systems, USA), and special microfluidic lids for Falcon tubes (Elvesys, France), which can be used with standard high-pressure liquid chromatography connectors and polytetrafluoroethylene tubing. Elastic tubing (C-Flex, Cole-Parmer, USA) was used in combination with the pinch valves.

Electrical Impedance Measurement: A commercial impedance analyzer (HP4248A) in combination with an electrical switch (Keithley 7001 switch system) was used for measuring the electrical impedance spectrum between both electrodes of the microfluidic cartridge in the range between 100 Hz and 100 kHz. Electrical connection of the microfluidic module with the impedance measuring system was carried out by commercial connectors that were soldered onto the contact pads of the cartridge. A LabView program controls data acquisition and impedance data were recorded in time intervals of 10 min.

System Integration of the Microfluidic Platform: All subsystems described form one module of the microfluidic platform. The miniaturized incubator microscope with the microfluidic cartridge was integrated with the fluidic circuit and connected to the impedance measurement system. The flexible modular platform concept allows for the individual operation of one single module and for the interconnection of multiple modules (Figure 6). Control of the microfluidic module was performed by a custom made electronic instrumentation. It provides a universal serial bus (USB) communication interface to support microfluidic valves handling by corresponding graphical user interface (GUI) software.

Reagents for Nanoparticle Synthesis: Silver nitrate ($AgNO_3$), Gold(III) chloride trihydrate ($HAuCl_4 \cdot 3H_2O$, 99%), trisodium citrate ($Na_3C_6H_5O_7$), and tannic acid ($C_{76}H_{52}O_{46}$), poly(ethylene glycol) methyl ether thiol (mol wt 5000), tetraethyl orthosilicate (TEOS, ≥ 98%), 3-(aminopropyl) triethoxysilane (APTES, ≥ 98%), fluorescein 5(6)-isothiocyanate (FITC, ≥ 90%), hydrochloric acid ACS reagent (HCl, 37%), sodium hydroxide BioXtra, ≥ 98% (acidimetric) pellets (anhydrous), tetramethylammonium hydroxide (TMAOH) solution ACS reagent with a concentration 1.0 ± 0.02 M in water and *cis*-diammineplatinum(II) dichloride, were purchased from Sigma-Aldrich. Ammonia solution (ACS Reagent, p.a. 28–30%) and dried ethanol (seccoSolv max 0.01% H_2O) were purchased from Merck and titanium(IV) isopropoxide 97%, was purchased from Fluka Chemika. Triton X-100 was purchased from Applichem, FDA and PI from Invitrogen. All chemicals were used as received without further purification. Distilled water passed through a Millipore system (ρ = 18.2 MΩ) was used in all experiments. All glassware was first rinsed with acetone and then with Millipore water before use.

Synthesis of Silver Nanoparticles (Ag-NP): Silver nanoparticles of ≈20 nm in diameter were prepared by the seeded-growth method recently reported by Bastús et al.[97] In a typical experiment, 100 mL volume of an aqueous solution containing sodium citrate (SC, 5×10^{-3} M) and tannic acid (TA, 0.1×10^{-3} M) was prepared and heated up to 100 °C with a heating mantle in a three-neck round-bottomed flask for 15 min under vigorous stirring. A condenser was used to prevent the evaporation of the solvent. After boiling had commenced, $AgNO_3$ (1 mL, 25×10^{-3} M) of was injected into this solution. The solution became bright yellow immediately indication the formation of the silver seeds. Immediately after the synthesis of Ag seeds and in the same vessel, the synthesized silver seeds were grown by cooling down the solution to 90 °C, the seed solution was diluted by extracting 20 mL of sample and adding Milli-Q-water (17 mL) and then SC (500 µL, 25×10^{-3} M), TA (1.5 mL, 2.5×10^{-3} M), and $AgNO_3$ (1 mL, 25×10^{-3} M) were sequentially injected, again. This process was repeated up to two times, progressively growing the size of the Ag-NP until reaching the desired size ≈ 20 nm (≈ 1.8×10^{12} NP mL^{-1}). The obtained Ag-NP were purified by centrifugation and stored in a solution containing both TA and SC.

Synthesis of Silica Dioxide –FITC Core Labeled Nanoparticles (SiO_2-FITC NP): Core labeled silica nanoparticles with the fluorophore FITC were prepared by following and adapting the method reported by van Blaaderen et al.[98] First, the silane-dye precursor was prepared. For this purpose, in a 100 mL flask, the FITC was measured accurately and dissolved in dry ethanol (50 mL). Then, the APTES was added under stirring and the flask was sealed using septum and left for 15 min under an argon atmosphere in dark conditions. Finally, the reaction was left for 24 h under magnetic agitation. Once the precursor was prepared, in a flask sealed with the help of a septum and under argon atmosphere, dry ethanol (45 mL) was added. Then, after 10 min of stirring, 2.02 mL (50.7 mmol) of ammonium hydroxide 28% was added and left for 5 min with continuous stirring. Finally, TEOS (1.7 mL, 7.6 mmol) and APTES-FITC precursor (5 mL) were sequentially added in the ethanol anhydride solution whilst maintaining a constant solvent volume. The reaction was left for 24 h stirring in dark conditions. Dialysis was used to purify unreacted dye and precursor. All the above experiments were conducted at room temperature.

Synthesis of Titanium Dioxide Nanoparticles (TiO_2-NP): Titanium anatase nanoparticles of mean size ≈ 4 nm in diameter were prepared by a precipitation method following and adapting the method reported by Pottier et al.[99] The adapted method is described in Elje et al.[83] Samples were further purified by three centrifuging cycles and resuspended in an aqueous solution of Tetramethylammonium hydroxide (TMAOH, 100 mol L^{-1}). Afterwards they were characterized by transmission electron microscopy (TEM), dynamic light scattering, and UV–vis spectroscopy. The former was used to determine the particle size and to characterize the crystallinity of particles.

Synthesis of Polyethylene Glycol-Coated Gold Nanoparticles (Au-PEG-NP): Gold nanoparticles of ≈10 nm in diameter were prepared by the citrated-stabilized seeded-growth method reported by Bastús et al.[100] A solution of 2.2×10^{-3} M sodium citrate in Milli-Q water (150 mL) was heated with a heating mantle in a 250 mL three-necked round-bottomed flask for 15 min under vigorous stirring. A condenser was utilized to prevent the evaporation of the solvent. After boiling had commenced, 1 mL of $HAuCl_4$ (25×10^{-3} M) was injected. The color of the solution changed from yellow to bluish-grey and then to soft pink in 10 min. The resulting particles (≈10 nm, ≈3×10^{12} NPs mL^{-1}) are coated with negatively charged citrate ions and hence are well suspended in H_2O. Immediately after the synthesis of the Au seeds and in the same reaction vessel, the reaction was cooled and NPs were conjugated directly with a thiol-PEG MW5000 solution to a final concentration of 2×10^{-6} M and was left overnight with gently stirring, to assure the complete coating of the Au NPs. Finally, the obtained PEGylated Au-NP were purified by centrifugation and dispersed in water, to remove the unbound PEG and the free citrate molecules.

UV–vis Spectroscopy: UV–visible spectra were acquired with an Agilent Cary 60 UV–vis spectrophotometer as described in Elje et al.[83]

Transmission Electron Microscopy: TEM diameter of the synthesized nanoparticles was obtained from the analysis of TEM images (Figure 3) acquired with an FEI Tecnai G2 F20 S-TWIN HR(S) TEM equipped with energy-dispersive X-ray spectroscopy detector, operated at an accelerated voltage of 200 kV. Microliters of the samples were prepared by drop-casting 10 µL of the sample on a carbon-coated copper TEM grid and left to dry at room temperature. Scanning electron microscopy (SEM) was conducted using an FEI Magellan 400L XHR SEM, in scanning mode operated at 1 kV and in transmission mode operated at 20 kV. Scanning transmission electron microscopy was used for bigger sizes. Average size and size distribution of the samples were measured using ImageJ software by counting at least 300 particles from different regions of the grid.

Dynamic Light Scattering: Dynamic light scattering and laser Doppler anemometry were used to determine the hydrodynamic size and the surface charge of the nanoparticles as reported by Elje et al.[83]

Induced Coupled Plasma-Mass Spectroscopy: ICP-MS was performed using an ICP-MS Perkin Elmer (model: NexION 300). For ICP-MS analysis, the nanoparticles were dissolved in concentrated *aqua regia*, which was then heated to ensure complete dissolution of all the metals and diluted to an optimal concentration for ICP-MS analysis. The

samples for ICP-MS measurements were prepared as follows: First, the colloidal solution containing the nanoparticles was centrifuged at 40.000 g for 45 min. The supernatant and the pellet were then analyzed separately.

Cell Lines and Standard Cell Cultivation: All cell culture reagents were obtained from Invitrogen (Karlsruhe, Germany), unless stated otherwise. The human lung epithelial carcinoma cells A549 (ATCC CCL-185), the human lung bronchial epithelial cells 16HBE (SCC150, Merck, Darmstadt, Germany) and the human hepatocarcinoma cells HepG2 (ATCC HB-8065) were cultured in Roswell Park Memorial Institute (RPMI) 1640 medium supplemented with L-glutamine (4×10^{-3} M), penicillin (100 U mL^{-1}), streptomycin (100 µg mL^{-1}), and 10% (v/v) fetal calf serum (FCS), as previously described in Kohl et al.[82] The human renal proximal tubule epithelial (TH-1) cells obtained from Kerafast were cultivated in Dulbecco's Modified Eagle's Medium (DMEM) supplemented with penicillin (100 U mL^{-1}), streptomycin (100 µg mL^{-1}), and 10% FCS as described in Sramkova et al.[101] In cocultivation experiments TH-1 cells were cultured in RPMI 1640 medium as all other cell lines. Cells were maintained in a 5% CO_2 humidified atmosphere at 37 °C.

Cell Cultivation and NP Exposure in a Single Microfluidic Platform Module: The cells were trypsinized and diluted in cell culture medium to 2×10^6 cells mL^{-1}. The cell solution was manually delivered into the cavity of the microincubator by a syringe. After 2 h of adherence, the tubing of the syringe pump was connected to the microfluidic incubator module and fresh cell culture medium was constantly pumped through the micro incubator at a flow rate of 100 µL h^{-1}. After 24 h of cultivation the cells were treated with the test substances. 24 h exposures with cis-Pt, SiO_2-FITC-NP and Ag-NP were performed with this experimental setup.

Cell Cultivation and NP Exposure in Interconnected Microfluidic Platform Modules: Two single modules were combined using one tubing system. The cells were prepared as described above. Just before cell exposure the medium syringe of module 1 was replaced by a syringe with the test substance (20 µg mL^{-1} cis-Pt or 100 µg mL^{-1} SiO_2-FITC-NP) and the microfluidics of the two models guaranteed a constant flow of the test substance in both modules. 24 h exposures with cis-Pt and SiO_2-FITC-NP were performed with this experimental setup.

Electrochemical Cell Characterization (Impedance Measurement): Impedance spectra were recorded at different frequencies between 100 Hz and 10 kHz in order to characterize barrier integrity during treatment with test substances. Impedance values were measured every 10 min. Based on previous findings with microhole array membranes, 10 kHz was selected as an appropriate measurement frequency Kurz et al.[102]

Live/Dead Staining: The cells were stained with FDA and PI to allow for visualization of live and dead cells, respectively. The cells were incubated in the cartridge with FDA (30 µg mL^{-1}) and PI (40 µg mL^{-1}) for up to 1 min, before washing with phosphate buffered saline (PBS) and imaging via the miniaturized microscope. The recorded fluorescence images were visually analyzed using GIMP.

Comet Assay after Experiments in Cartridge: After live/dead staining at the end of the culture period, cells from the microfluidic cartridge were detached by trypsinization (0.25%) for 10 min. The cells were resuspended in culture medium and centrifuged (5 min, 200 g, 21 °C), before the cell number was counted in Countess (Invitrogen) with trypan-blue staining, and the DNA damage was measured by the comet assay.

The miniaturized 12-gel modified comet assay was performed as described by El Yamani et al.,[103] with the bacterial repair enzyme formamidopyrimidine DNA glycosylase (Fpg, gift from Professor Andrew Collins, University of Oslo, Norway), which converts oxidized (majority of it is 8-oxoG) or alkylated purine bases to SBs[84,103,104] for detection of oxidized or alkylated bases. Cell cultures were disaggregated as explained above. As reported by Elje et al.[100] the cell suspension was mixed in ratio 1:3 with low melting point-agarose (0.8% w/v, A9414, Sigma-Aldrich, 37 °C) giving a final agarose concentration of 0.6% w/v, and mini-gels (10 µL) were made on microscope slides precoated with 0.5% standard melting point agarose (05066, Sigma-Aldrich). The samples were submerged in lysis solution (2.5 M NaCl, 0.1 M ethylenediaminetetraacetic acid (EDTA), 10×10^{-3} M Tris, 10% v/v Triton X-100, pH 10.4) for at least 1 h. As a control for SBs, separate slides were submerged in 100×10^{-6} M H_2O_2 in PBS for 5 min at 4 °C, washed twice for 2 min in PBS (4 °C) and then submerged in a separate coplin jar of lysis solution.

After lysis, slides for Fpg treatment were washed twice for 8 min in buffer F (40×10^{-3} M 4-(2-hydroxyethyl)-1-piperazineethanesulfonic acid (HEPES), 0.1 M KCl, 0.5×10^{-3} M EDTA, 0.2 mg mL^{-1} bovine serum albumin (BSA), pH 8.4), added Fpg diluted in buffer F, and covered with a polyethylene foil and incubated at 37 °C for 30 min in a humid box. As positive control for function of Fpg, reference samples were included; A549 cells exposed to the photosensitizer Ro 19–8022 (Hoffmann La Roche, Switzerland), which with light induces oxidized purines, mainly 8-oxoG, which is detected by the Fpg.[104,105] A549 cells were exposed to Ro 19-8022 (2×10^{-6} M) and irradiated with visible light (30 cm distance from cells, 250 W) on ice for 4 min, before freezing of aliquots and embedding into gels on day of experiment.

After Fpg treatment, slides with cells embedded in gels were placed in the electrophoresis tank, submerged in electrophoresis solution (0.3 M NaOH, 1×10^{-3} M EDTA, pH > 13.4) for 20 min to let the DNA unwind, before running electrophoresis for 20 min (25 V, 1.25 V cm^{-1}, Consort EV202). The gels were neutralized in PBS, washed in ultrapure water and left to dry overnight. Comets were visualized after staining with SYBR gold (1:2000, S11494, Sigma-Aldrich), and scored in Leica DMI 6000 B (Leica Microsystems), equipped with an SYBRphotographic filter (Thermo Fischer Scientific) using the software Comet assay IV 4.3.1 (Perceptive Instruments, Bury St Edmunds, UK). Median DNA tail intensity was calculated from 50 comets per gel as a measure of DNA SBs, with a total of three gels and 150 comets per chip sample and two gels and 100 comets per reference sample.

Viability Assay (alamarBlue) in 96-Well Plates: Cells were seeded at a density of 2×10^4 per well into a 96-well plate and cultured for 24 h in cell culture medium. Exponentially growing cells were then preincubated, in the presence of test compounds or untreated (control) cells, for 24 h. After treatment, cells were incubated with 100 µL of working solution of alamarBlue (Invitrogen, USA) for 4 h according to the manufacturer's protocol. The fluorescence (excitation 530 nm, emission 590 nm) in each well was measured on a microplate reader (POLARStar OPTIMA, BMG LABTECH). EC_{50} values were calculated based on the alamarBlue results.

Transport Studies under Static Conditions: 16HBE cells (8.0×10^4 per well) were seeded into a 12-well cell culture insert (order# 3460, Corning) and cultured for 4 d in cell culture medium. Via CellZScope the impedance was measured continuously. At an impedance value > 600 Ω/cm^2 the cells were exposed to Au-PEG-NPs (5.0 µg mL^{-1}). After 4, 24 and 48 h the NP-containing cell culture media on the apical and basolateral side was removed and used for ICP MS analysis to determine the amount of Au in the sample. Before analysis the NPs were dissolved in aqua regia, which was heated to ensure complete dissolution of all metals. 200 µL of the cell culture media was diluted to a final volume of 10 mL. Cells were harvested, digested, and diluted to a volume of 5 mL. ICP-MS was performed using an ICP-MS Perkin Elmer (Model NexION 300).

Transport Studies under Fluidic Conditions: 16HBE cells (4×10^6 mL^{-1}) were injected in the microfluidic cartridge and cultured for 24 h in cell culture medium (flow rate 100 µL h^{-1}). The impedance was measured continuously. After the impedance reached a constant value the cells were exposed to Au-PEG-NPs (5.0 µg mL^{-1}, in cell culture medium). During the 4 h, 24 h, and 48 h exposure the NP-containing cell culture media on the apical side was collected in a tube and prepared for atomic spectroscopy to determine the amount of Au in the sample. Before analysis the NPs were dissolved in pure water which was heated to ensure complete dissolution of all metals. Throughout the experiments water from NANOpure system (Wilhelm Werner GmbH, Germany) was used. The atomic absorption spectrometry (AAS) measurements were performed at 242.8 nm using a high-resolution continuum source atomic absorption spectrometer AA700 (Analytik Jena AG, Jena, Germany). As a stock solution for AAS calibration, standard 1.000 g L^{-1} Au solution was used. The limit of detection was determined to be lower than 0.125 µg L^{-1}. The amount of Au in the sample was calculated as µg L^{-1}.

Supporting Information

Supporting Information is available from the Wiley Online Library or from the author.

Acknowledgements

T.K. and Y.K. contributed equally to this work. The authors thank Frank Bauerfeld for system assembly and electrical testing, Werner Haberer for assembly of the microfluidic cartridges, Axel Brenner for the fabrication of the silicon micro cavity chips, Hoffman La Roche for providing the Ro 19-8022, NorGenoTech for providing the Fpg enzyme, and Karen Steenson for proofreading. This research was funded by the European Commission under the Horizon2020 programme (HISENTS, Grant Agreement No. 685817 and VISION, Grant Agreement No. 857381); and by the Norwegian Research Council Norway (RCN) via the European Research Area Network (ERA-NET) EuroNanoMed II project INNOCENT (RCN 271075) and the ERA-NET EuroNanoMed III project Graphene-encapsulated magnetic nanoparticles (RCN 246672/O70). K.K. received Short Term Scientific Mission Grant (ID 42926) under COST Action CA 17140 "Cancer Nanomedicine from the Bench to the Bedside" supported by COST (European Cooperation in Science and Technology). E.E. received funding from the Norwegian Research Council (272412/F40). O.H.M. received funding from the Spanish Ministry of Economy and Competitiveness (SEV-2013-0295-17-3).

Open access funding enabled and organized by Projekt DEAL.

Conflict of Interest

The authors declare no conflict of interest.

Keywords

drug efficiency, in vitro culture-on-chip, microfluidic platform, miniaturized incubator microscope, (nano)safety

Received: September 25, 2020
Revised: December 18, 2020
Published online:

[1] European Comission, Regulation (EC) No 1907/2006 – Registration, Evaluation, Authorisation and Restriction of Chemicals (REACH) – EU-OSHA, https://osha.europa.eu/de/legislation/directives/regulation-ec-no-1907–2006-of-the-european-parliament-and-of-the-council, (accessed: November 2020)
[2] N. Ashammakhi, K. Wesseling-Perry, A. Hasan, E. Elkhammas, Y. S. Zhang, *Kidney Int.* **2018**, *94*, 1073.
[3] N. Alépée, A. Bahinski, M. Daneshian, B. De Wever, E. Fritsche, A. Goldberg, J. Hansmann, T. Hartung, J. Haycock, H. Hogberg, L. Hoelting, J. M. Kelm, S. Kadereit, E. McVey, R. Landsiedel, M. Leist, M. Lübberstedt, F. Noor, C. Pellevoisin, D. Petersohn, U. Pfannenbecker, K. Reisinger, T. Ramirez, B. Rothen-Rutishauser, M. Schäfer-Korting, K. Zeilinger, M.-G. Zurich, *ALTEX* **2014**, *31*, 441.
[4] Q. Ramadan, M. A. M. Gijs, *Lab Chip* **2015**, *15*, 614.
[5] D. Bovard, A. Sandoz, K. Luettich, S. Frentzel, A. Iskandar, D. Marescotti, K. Trivedi, E. Guedj, Q. Dutertre, M. C. Peitsch, J. Hoeng, *Lab Chip* **2018**, *18*, 3814.
[6] A. Bein, W. Shin, S. Jalili-Firoozinezhad, M. H. Park, A. Sontheimer-Phelps, A. Tovaglieri, A. Chalkiadaki, H. J. Kim, D. E. Ingber, *Cell. Mol. Gastroenterol. Hepatol.* **2018**, *5*, 659.
[7] J. D. Stucki, N. Hobi, A. Galimov, A. O. Stucki, N. Schneider-Daum, C.-M. Lehr, H. Huwer, M. Frick, M. Funke-Chambour, T. Geiser, O. T. Guenat, *Sci. Rep.* **2018**, *8*, 14359.
[8] L. Elberskirch, T. Knoll, A. Moosmann, N. Wilhelm, H. von Briesen, S. Wagner, *J. Drug Delivery Sci. Technol.* **2019**, *54*, 101248.
[9] I. Maschmeyer, A. K. Lorenz, K. Schimek, T. Hasenberg, A. P. Ramme, J. Hübner, M. Lindner, C. Drewell, S. Bauer, A. Thomas, N. S. Sambo, F. Sonntag, R. Lauster, U. Marx, *Lab Chip* **2015**, *15*, 2688.
[10] E.-M. Materne, A. P. Ramme, A. P. Terrasso, M. Serra, P. M. Alves, C. Brito, D. A. Sakharov, A. G. Tonevitsky, R. Lauster, U. Marx, *J. Biotechnol.* **2015**, *205*, 36.
[11] J. Lee, S. Kim, *Curr. Drug Metab.* **2018**, *19*, 577.
[12] D. T. Phan, R. H. F. Bender, J. W. Andrejecsk, A. Sobrino, S. J. Hachey, S. C. George, C. C. Hughes, *Exp. Biol. Med.* **2017**, *242*, 1669.
[13] G. Mazzoleni, D. Di Lorenzo, N. Steimberg, *Genes Nutr.* **2009**, *4*, 13.
[14] R. Mittal, F. W. Woo, C. S. Castro, M. A. Cohen, J. Karanxha, J. Mittal, T. Chhibber, V. M. Jhaveri, *J. Cell. Physiol.* **2019**, *234*, 8352.
[15] M. W. van der Helm, A. D. van der Meer, J. C. T. Eijkel, A. van den Berg, L. I. Segerink, *Tissue Barriers* **2016**, *4*, e1142493.
[16] A. Ehrlich, D. Duche, G. Ouedraogo, Y. Nahmias, *Annu. Rev. Biomed. Eng.* **2019**, *21*, 219.
[17] J. Shrestha, S. Razavi Bazaz, H. Aboulkheyr Es, D. Yaghobian Azari, B. Thierry, M. Ebrahimi Warkiani, M. Ghadiri, *Crit. Rev. Biotechnol.* **2020**, *40*, 213.
[18] *Test No. 439*: *In Vitro Skin Irritation: Reconstructed Human Epidermis Test Method*, OECD **2020**.
[19] *Test No. 492*: *Reconstructed Human Cornea-like Epithelium (RhCE) Test Method for Identifying Chemicals Not Requiring Classification and Labelling for Eye Irritation or Serious Eye Damage*, OECD **2019**.
[20] *Test No. 431*: *In Vitro Skin Corrosion: Reconstructed Human Epidermis (RHE) Test Method*, OECD **2013**.
[21] *Test No. 432*: *In Vitro 3T3 NRU Phototoxicity Test*, OECD **2019**.
[22] *Test No. 490*: *In Vitro Mammalian Cell Gene Mutation Tests Using the Thymidine Kinase Gene*, OECD **2015**.
[23] *Test No. 476*: *In Vitro Mammalian Cell Gene Mutation Test*, OECD Publishing **1997**.
[24] C. Giese, U. Marx, *Adv. Drug Delivery Rev.* **2014**, *69–70*, 103.
[25] J. Hogan, *Nature* **2006**, *442*, 351.
[26] C. Luni, E. Serena, N. Elvassore, *Curr. Opin. Biotechnol.* **2014**, *25*, 45.
[27] L. Richter, V. Charwat, C. Jungreuthmayer, F. Bellutti, H. Brueckl, P. Ertl, *Lab Chip* **2011**, *11*, 2551.
[28] P. Yager, T. Edwards, E. Fu, K. Helton, M. R. KristenNelson Tam, B. H. Weigl, *Nature* **2006**, *442*, 412.
[29] R. Daw, J. Finkelstein, *Nature* **2006**, *442*, 367.
[30] K. Yum, S. G. Hong, K. E. Healy, L. P. Lee, *Biotechnol. J.* **2014**, *9*, 16.
[31] B. Zhang, M. Radisic, *Lab Chip* **2017**, *17*, 2395.
[32] H. Kimura, T. Ikeda, H. Nakayama, Y. Sakai, T. Fujii, *J. Lab. Autom.* **2015**, *20*, 265.
[33] S. N. Bhatia, D. E. Ingber, *Nat. Biotechnol.* **2014**, *32*, 760.
[34] E.-M. Materne, I. Maschmeyer, A. K. Lorenz, R. Horland, K. M. S. Schimek, M. Busek, F. Sonntag, R. Lauster, U. Marx, *J. Visualized Exp.* **2015**, *98*, e52526.
[35] M. Rothbauer, H. Zirath, P. Ertl, *Lab Chip* **2018**, *18*, 249.
[36] M. Rothbauer, J. M. Rosser, H. Zirath, P. Ertl, *Curr. Opin. Biotechnol.* **2019**, *55*, 81.
[37] B. Bachmann, S. Spitz, M. Rothbauer, C. Jordan, M. Purtscher, H. Zirath, P. Schuller, C. Eilenberger, S. F. Ali, S. Mühleder, E. Priglinger, M. Harasek, H. Redl, W. Holnthoner, P. Ertl, *Biomicrofluidics* **2018**, *12*, 042216.
[38] R. Booth, H. Kim, *Lab Chip* **2012**, *12*, 1784.

[39] D. Mandt, P. Gruber, M. Markovic, M. Tromayer, M. Rothbauer, S. R. A. Krayz, F. Ali, J. Van Hoorick, W. Holnthoner, S. Mühleder, P. Dubruel, S. Van Vlierberghe, P. Ertl, R. Liska, A. Ovsianikov, *Int. J. Bioprint.* **2018**, *4*, 144.
[40] C. Drieschner, S. Könemann, P. Renaud, K. Schirmer, *Lab Chip* **2019**, *19*, 3268.
[41] A. Artzy-Schnirman, N. Hobi, N. Schneider-Daum, O. T. Guenat, C.-M. Lehr, J. Sznitman, *Eur. J. Pharm. Biopharm.* **2019**, *144*, 11.
[42] S. Ehrmann, O. Schmid, C. Darquenne, B. Rothen-Rutishauser, J. Sznitman, L. Yang, H. Barosova, L. Vecellio, J. Mitchell, N. Heuze-Vourc'h, *Expert Opin. Drug Delivery* **2020**, *17*, 463.
[43] L. J. van den Broek, L. I. J. C. Bergers, C. M. A. Reijnders, S. Gibbs, *Stem Cell Rev. Rep.* **2017**, *13*, 418.
[44] A. Bal-Öztürk, B. Miccoli, M. Avci-Adali, F. Mogtader, F. Sharifi, B. Çeçen, G. Yaşayan, D. Braeken, E. Alarcin, *Curr. Pharm. Des.* **2018**, *24*, 5437.
[45] A. Grassart, V. Malardé, S. Gobaa, A. Sartori-Rupp, J. Kerns, K. Karalis, B. Marteyn, P. Sansonetti, N. Sauvonnet, *Cell Host Microbe* **2019**, *26*, 435.
[46] M. Maurer, M. S. Gresnigt, A. Last, T. Wollny, F. Berlinghof, R. Pospich, Z. Cseresnyes, A. Medyukhina, K. Graf, M. Gröger, M. Raasch, F. Siwczak, S. Nietzsche, I. D. Jacobsen, M. T. Figge, B. Hube, O. Huber, A. S. Mosig, *Biomaterials* **2019**, *220*, 119396.
[47] K. Kulthong, L. Duivenvoorde, H. Sun, S. Confederat, J. Wu, B. Spenkelink, L. de Haan, V. Marin, M. van der Zande, H. Bouwmeester, *Toxicol. In Vitro* **2020**, *65*, 104815.
[48] M. Gröger, J. Dinger, M. Kiehntopf, F. T. Peters, U. Rauen, A. S. Mosig, *Adv. Healthcare Mater.* **2018**, *7*, 1700616 https://doi.org/10.1002/adhm.201700616.
[49] J. Deng, Z. Chen, X. Zhang, Y. Luo, Z. Wu, Y. Lu, T. Liu, W. Zhao, B. Lin, *Biomed. Microdevices* **2019**, *21*, 57.
[50] K. H. Dodson, F. D. Echevarria, D. Li, R. M. Sappington, J. F. Edd, *Biomed. Microdevices* **2015**, *17*, 114.
[51] H. J. Kim, D. E. Ingber, *Integr. Biol.* **2013**, *5*, 1130.
[52] E. Chin, E. Goh, *Methods Cell Biol.* **2018**, *146*, 159.
[53] T. T. G. Nieskens, M. J. Wilmer, *Eur. J. Pharmacol.* **2016**, *790*, 46.
[54] K. Achberger, C. Probst, J. Haderspeck, S. Bolz, J. Rogal, J. Chuchuy, M. Nikolova, V. Cora, L. Antkowiak, W. Haq, N. Shen, K. Schenke-Layland, M. Ueffing, S. Liebau, P. Loskill, *Elife* **2019**, *8*, e46188.
[55] L. Boeri, L. Izzo, L. Sardelli, M. Tunesi, D. Albani, C. Giordano, *Bioengineering (Basel, Switzerland)* **2019**, *6*, 91 https://doi.org/10.3390/bioengineering6040091.
[56] T. Satoh, S. Sugiura, K. Shin, R. Onuki-Nagasaki, S. Ishida, K. Kikuchi, M. Kakiki, T. Kanamori, *Lab Chip* **2017**, *18*, 115.
[57] J. H. Sung, *Methods Cell Biol.* **2018**, *146*, 183.
[58] I. Wagner, E.-M. Materne, S. Brincker, U. Süssbier, C. Frädrich, M. Busek, F. Sonntag, D. A. Sakharov, E. V. Trushkin, A. G. Tonevitsky, R. Lauster, U. Marx, *Lab Chip* **2013**, *13*, 3538.
[59] J. H. Sung, M. B. Esch, J.-M. Prot, C. J. Long, A. Smith, J. J. Hickman, M. L. Shuler, *Lab Chip* **2013**, *13*, 1201.
[60] Y. Temiz, R. D. Lovchik, G. V. Kaigala, E. Delamarche, *Microelectron. Eng.* **2015**, *132*, 156.
[61] T. H. Park, M. L. Shuler, *Biotechnol. Prog.* **2003**, *19*, 243.
[62] Y. Tanaka, K. Sato, T. Shimizu, M. Yamato, T. Okano, T. Kitamori, *Biosens. Bioelectron.* **2007**, *23*, 449.
[63] J. El-Ali, P. K. Sorger, K. F. Jensen, *Nature* **2006**, *442*, 403.
[64] S. Petronis, M. Stangegaard, C. Bovöge Christensen, M. Dufva, *BioTechniques* **2006**, *40*, 368.
[65] P. Shah, A. Kaushik, X. Zhu, C. Zhang, C.-Z. Li, *Analyst* **2014**, *139*, 2088.
[66] H. A. Alhadrami, *Biotechnol. Appl. Biochem.* **2018**, *65*, 497.
[67] T. Sun, E. J. Swindle, J. E. Collins, J. A. Holloway, D. E. Davies, H. Morgan, *Lab Chip* **2010**, *10*, 1611.
[68] A. Susloparova, D. Koppenhöfer, J. K. Y. Law, X. T. Vu, S. Ingebrandt, *Lab Chip* **2015**, *15*, 668.
[69] O. Y. F. Henry, R. Villenave, M. J. Cronce, W. D. Leineweber, M. A. Benz, D. E. Ingber, *Lab Chip* **2017**, *17*, 2264.
[70] Y. Mermoud, M. Felder, J. D. Stucki, A. O. Stucki, O. T. Guenat, *Sens. Actuators, B* **2018**, *255*, 3647.
[71] T. Sun, S. Tsuda, K.-P. Zauner, H. Morgan, *Biosens. Bioelectron.* **2010**, *25*, 1109.
[72] J. Kahle, R. Levin, W. Niles, B. Rasnow, M. Schehlein, C. Shumate, *J. Assoc. Lab. Autom.* **2010**, *15*, 355.
[73] S. R. Heidemann, P. Lamoureux, K. Ngo, M. Reynolds, R. E. Buxbaum, *BioTechniques* **2003**, *35*, 708.
[74] M. M. Frigault, J. Lacoste, J. L. Swift, C. M. Brown, *J. Cell Sci.* **2009**, *122*, 753.
[75] L. Lin, S.-S. Wang, M.-H. Wu, C.-C. Oh-Yang, *Sensors (Basel)* **2011**, *11*, 8395.
[76] S. K. Mahto, V. Charwat, P. Ertl, B. Rothen-Rutishauser, S. W. Rhee, J. Sznitman, *Nanotoxicology* **2015**, *9*, 381.
[77] C. Rassie, J. Van Wyk, L. Wilson, N. Ntshongontshi, A. Jonnas, U. Feleni, R. F. Ajayi, P. Baker, E. Iwuoha, *J. Nano Res.* **2017**, *45*, 164.
[78] A. Jaitovich, S. Mehta, N. Na, A. Ciechanover, R. D. Goldman, K. M. Ridge, *J. Biol. Chem.* **2008**, *283*, 25348.
[79] R. Baudoin, L. Griscom, J. M. Prot, C. Legallais, E. Leclerc, *Biochem. Eng. J.* **2011**, *53*, 172.
[80] N. A. Stathopoulos, J. D. Hellums, *Biotechnol. Bioeng.* **1985**, *27*, 1021.
[81] L. Kim, Y. C. Toh, J. Voldman, H. Yu, *Lab Chip* **2007**, *7*, 681.
[82] Y. Kohl, G. J. Oostingh, A. Sossalla, A. Duschl, H. von Briesen, H. Thielecke, *Nanoscale Res. Lett.* **2011**, *6*, 505.
[83] E. Elje, E. Mariussen, O. H. Moriones, N. G. Bastús, V. Puntes, Y. Kohl, M. Dusinska, E. Rundén-Pran, *Nanomaterials* **2020**, *10*, 545 https://doi.org/10.3390/nano10030545.
[84] E. Elje, M. Hesler, E. Rundén-Pran, P. Mann, E. Mariussen, S. Wagner, M. Dusinska, Y. Kohl, *Mutat. Res., Toxicol. Environ. Mutagen.* **2019**, *845*, 403033.
[85] B. Srinivasan, A. R. Kolli, M. B. Esch, H. E. Abaci, M. L. Shuler, J. J. Hickman, *J. Lab. Autom.* **2015**, *20*, 107.
[86] P. Miranda-Azpiazu, S. Panagiotou, G. Jose, S. Saha, *Sci. Rep.* **2018**, *8*, 8784.
[87] Q. Ramadan, F. C. W. Ting, *Lab Chip* **2016**, *16*, 1899.
[88] A. Skardal, S. V Murphy, M. Devarasetty, I. Mead, H.-W. Kang, Y.-J. Seol, Y. Shrike Zhang, S.-R. Shin, L. Zhao, J. Aleman, A. R. Hall, T. D. Shupe, A. Kleensang, M. R. Dokmeci, S. Jin Lee, J. D. Jackson, J. J. Yoo, T. Hartung, A. Khademhosseini, S. Soker, C. E. Bishop, A. Atala, *Sci. Rep.* **2017**, *7*, 8837.
[89] U. Marx, T. B. Andersson, A. Bahinski, M. Beilmann, S. Beken, F. R. Cassee, M. Cirit, M. Daneshian, S. Fitzpatrick, O. Frey, C. Gaertner, C. Giese, L. Griffith, T. Hartung, M. B. Heringa, J. Hoeng, W. H. de Jong, H. Kojima, J. Kuehnl, M. Leist, A. Luch, I. Maschmeyer, D. Sakharov, A. J. A. M. Sips, T. Steger-Hartmann, D. A. Tagle, A. Tonevitsky, T. Tralau, S. Tsyb, A. van de Stolpe, R. Vandebriel, P. Vulto, J. Wang, J. Wiest, M. Rodenburg, A. Roth, *ALTEX* **2016**, *33*, 272.
[90] M. Mastrangeli, S. Millet, T. Orchid Partners, J. Van den Eijnden-van Raaij, *ALTEX* **2019**, *36*, 650.
[91] Y. S. Zhang, J. Aleman, S. R. Shin, T. Kilic, D. Kim, S. A. Mousavi Shaegh, S. Massa, R. Riahi, S. Chae, N. Hu, H. Avci, W. Zhang, A. Silvestri, A. Sanati Nezhad, A. Manbohi, F. De Ferrari, A. Polini, G. Calzone, N. Shaikh, P. Alerasool, E. Budina, J. Kang, N. Bhise, J. Ribas, A. Pourmand, A. Skardal, T. Shupe, C. E. Bishop, M. R. Dokmeci, A. Atala, A. Khademhosseini, *Proc. Natl. Acad. Sci. U. S. A.* **2017**, *114*, E2293.
[92] B. M. Maoz, A. Herland, O. Y. F. Henry, W. D. Leineweber, M. Yadid, J. Doyle, R. Mannix, V. J. Kujala, E. A. FitzGerald, K. K. Parker, D. E. Ingber, *Lab Chip* **2017**, *17*, 2294.
[93] P. M. Misun, J. Rothe, Y. R. F. Schmid, A. Hierlemann, O. Frey, *Microsyst. Nanoeng.* **2016**, *2*, 16022.

[94] C. Oleaga, C. Bernabini, A. S. T. Smith, B. Srinivasan, M. Jackson, W. McLamb, V. Platt, R. Bridges, Y. Cai, N. Santhanam, B. Berry, S. Najjar, N. Akanda, X. Guo, C. Martin, G. Ekman, M. B. Esch, J. Langer, G. Ouedraogo, J. Cotovio, L. Breton, M. L. Shuler, J. J. Hickman, *Sci. Rep.* **2016**, *6*, 20030.
[95] M. Hosokawa, A. Arakaki, M. Takahashi, T. Mori, H. Takeyama, T. Matsunaga, *Anal. Chem.* **2009**, *81*, 5308.
[96] J. Owen, M. Kuznecovs, R. Bhamji, N. William, N. Domenech-Garcia, M. Hesler, T. Knoll, Y. Kohl, A. Nelson, N. Kapur, *Rev. Sci. Instrum.* **2020**, *91*, 025002.
[97] N. G. Bastús, F. Merkoçi, J. Piella, V. Puntes, *Chem. Mater.* **2014**, *26*, 2836.
[98] A. Van Blaaderen, A. Vrij, *Langmuir* **1992**, *8*, 2921.
[99] A. Pottier, S. Cassaignon, C. Chanéac, F. Villain, E. Tronc, J.-P. Jolivet, *J. Mater. Chem.* **2003**, *13*, 877.
[100] N. G. Bastús, J. Comenge, V. Puntes, *Langmuir* **2011**, *27*, 11098.
[101] M. Sramkova, K. Kozics, V. Masanova, I. Uhnakova, F. Razga, V. Nemethova, P. Mazancova, L. Kapka-Skrzypczak, M. Kruszewski, M. Novotova, V. F. Puntes, A. Gabelova, *Mutat. Res., Toxicol. Environ. Mutagen.* **2019**, *845*, 403017.
[102] C. M. Kurz, A. Maurer, K. Thees, S. Schillberg, T. Velten, H. Thielecke, *Sens. Actuators, B* **2011**, *158*, 345.
[103] N. El Yamani, A. R. Collins, E. Rundén-Pran, L. M. Fjellsbø, S. Shaposhnikov, S. Zienolddiny, M. Dusinska, *Mutagenesis* **2017**, *32*, 117.
[104] A. R. Collins, *Methods Mol. Biol.* **2017**, *1641*, 173.
[105] A. Azqueta, J. Slyskova, S. A. S. Langie, I. O'Neill Gaivão, A. Collins, *Front. Genet.* **2014**, *5*, 288.